Geophysical Research Letters

RESEARCH LETTER
10.1029/2025GL120128

Impact of Continental Configuration on the Climate Response to Greenhouse-Gas Forcing in an Idealized GCM

David B. Bonan[1,2], **Marysa M. Laguë**[3], **and William R. Boos**[4,5]

[1]Department of Atmospheric and Climate Science, University of Washington, Seattle, WA, USA, [2]Cooperative Institute for Climate, Ocean, and Ecosystem Studies, University of Washington, Seattle, WA, USA, [3]Department of Geography, University of British Columbia, Vancouver, BC, Canada, [4]Department of Earth and Planetary Science, University of California, Berkeley, CA, USA, [5]Climate and Ecosystem Sciences Division, Lawrence Berkeley National Laboratory, Berkeley, CA, USA

Key Points:

- Land concentrated in the tropics reduces climate sensitivity, while extratropical land increases it via water-vapor and lapse-rate feedbacks
- Strong land-ocean warming contrasts occur when land is concentrated in polar regions or in a continuous meridional band from pole-to-pole
- Continental-configuration-dependent declines in land relative humidity arise from changes in oceanic moisture transport and land evaporation

Correspondence to:
D. B. Bonan,
dbonan@uw.edu

Citation:
Bonan, D. B., Laguë, M. M., & Boos, W. R. (2026). Impact of continental configuration on the climate response to greenhouse-gas forcing in an idealized GCM. *Geophysical Research Letters*, *53*, e2025GL120128. https://doi.org/10.1029/2025GL120128

Received 20 OCT 2025
Accepted 19 FEB 2026

Abstract The influence of continental configuration on the climate response to greenhouse-gas forcing remains poorly understood. Here, we use an idealized model with varying land-ocean coverage to investigate how the spatial distribution of land modulates the climate response to increased carbon-dioxide concentrations. When land is concentrated in tropical regions, equilibrium climate sensitivity is lower due to a weaker water-vapor feedback, land-ocean warming contrasts are minimal, and global-mean land relative humidity declines only slightly. By contrast, when land is concentrated in polar regions, equilibrium climate sensitivity is higher, land-ocean warming contrasts are pronounced, and global-mean land relative humidity declines substantially. Large land-ocean warming contrasts also occur when land is arranged in a continuous pole-to-pole meridional band. Changes in near-surface land relative humidity can be attributed to changes in land evaporation and oceanic moisture transport. Together, these results highlight the critical role of continental configuration in shaping Earth's climate response to greenhouse-gas forcing.

Plain Language Summary The distribution of land across Earth's surface has varied dramatically over geologic time, yet its influence on the climate system's response to greenhouse-gas forcing remains poorly understood. Using an idealized climate model, we show that the spatial distribution and orientation of land strongly shape Earth's response to increased atmosphere carbon dioxide concentrations. When most land is located in the tropics, higher carbon dioxide concentrations cause less overall warming, with land and ocean temperatures increasing by similar amounts and little drying over the global average land surface. In contrast, when most land is located outside of the tropics, higher carbon dioxide concentrations cause greater overall warming with amplified land warming and more pronounced drying over the global average land surface. We attribute these responses to distinct physical processes. These findings highlight the importance of continental configuration in modulating climate feedbacks and atmospheric hydrological responses to increased carbon dioxide concentrations, with implications for interpreting Earth's climate under different paleogeographic states.

1. Introduction

The distribution of land and ocean is a fundamental feature of Earth's present-day climate. Although land covers only about 30% of the Earth's surface, it is unevenly distributed: approximately 67% of the total landmass lies in the Northern Hemisphere, compared with approximately 33% in the Southern Hemisphere. This hemispheric asymmetry has long been recognized as an important factor influencing the climate system (e.g., Croll, 1870). Early studies that laid the foundation for contemporary climate models suggested that the larger land area in the Northern Hemisphere makes it more sensitive to increases in anthropogenic greenhouse gases (Manabe et al., 1991; Schneider & Thompson, 1981; Stouffer et al., 1989). Beyond this broad hemispheric contrast, however, it remains unclear how the geographic distribution of land more generally influences the sensitivity of global and regional climate to changes in greenhouse-gas concentrations.

Over the past billion years, Earth has experienced a wide range of continental configurations, from supercontinents near the equator to fragmented landmasses in the extratropics (Merdith et al., 2021; Müller et al., 2016; Scotese et al., 1988; Seton et al., 2012; Straume et al., 2020). Continental configuration is argued to be a major influence on the evolution of Earth's climate. For example, the opening of the Drake Passage (Barker & Burrell, 1977; Scher & Martin, 2006) has been suggested to enhance the ocean's global overturning circulation (Sijp & England, 2004; Toggweiler & Samuels, 1995), while the relative widths of the Atlantic and Pacific basins have

been associated with asymmetries in deep water formation between the basins (Ferreira et al., 2018; Jones & Cessi, 2017; Youngs et al., 2020). Yet the influence of continental configuration on the climate response to greenhouse-gas forcing remains relatively unexplored. Recent studies show that the extent of South America and its position relative to Africa affect the decline in Amazon precipitation under warming (Pietschnig et al., 2019, 2021), suggesting that continental geometry may play a first-order role in shaping the patterns of climate change. A key open question is how the latitude and orientation of landmasses influence other aspects of the climate response to elevated greenhouse-gas concentrations.

Addressing this question is particularly important because recent work has shown that continental configuration can strongly influence many aspects of the base climate state through atmospheric processes alone (Laguë et al., 2023). This suggests that land geometry may also modulate the climate response to greenhouse-gas forcing via purely atmospheric mechanisms. Under warming, land surfaces exhibit distinct features, including amplified warming relative to the ocean (Byrne & O'Gorman, 2013; Dong et al., 2009; Joshi et al., 2008; Manabe et al., 1991; Stouffer & Manabe, 1999) and widespread declines in near-surface relative humidity (Byrne & O'Gorman, 2016; Fu & Feng, 2014; Laîné et al., 2014; O'Gorman & Muller, 2010). However, it remains unclear whether the orientation of continents modulates these characteristic aspects of modern climate change. Because of the complexity of fully coupled Earth system models, isolating the role of land geometry remains challenging. A systematic evaluation of how differences in land configuration, including latitude and orientation, influence climate sensitivity and hydrological responses under greenhouse gas forcing is still needed.

In this study, we use an idealized atmospheric general circulation model (GCM) to investigate how different continental configurations shape Earth's climate response to increased greenhouse gases. When land is concentrated in tropical regions, equilibrium climate sensitivity is smaller, land-ocean warming contrasts are weaker, and global-mean near-surface land relative humidity declines only modestly. In contrast, when land is concentrated in polar regions, equilibrium climate sensitivity is larger, land-ocean warming contrasts are stronger, and global-mean near-surface land relative humidity decreases substantially. Large land-ocean warming contrasts also occur when land spans in a continuous meridional band from pole-to-pole. We interpret these responses using diagnostic energy and moisture budgets, yielding mechanistic insight into how continental configuration modulates climate sensitivity and informing interpretations of Earth's climate in different paleogeographic states.

2. Materials and Methods

2.1. Idealized GCM

To investigate the impact of continental configuration on the climate response to increased greenhouse-gas concentrations, we use the Model of an Idealized Moist Atmosphere (MiMA; Jucker & Gerber, 2017), an intermediate-complexity GCM made accessible through the Isca framework (Vallis et al., 2018). Simulations are performed at T42 horizontal resolution with 25 unequally spaced sigma levels, providing approximately 10 hPa spacing near the surface that gradually coarsens with height. The model includes a seasonal cycle in insolation (obliquity = 23.4398°, eccentricity = 0), a 360-day year, and a solar constant of 1360 W m^{-2}.

The atmosphere of MiMA includes moist dynamics and produces precipitation (Jucker & Gerber, 2017), but omits cloud radiative effects. MiMA is chosen because radiative transfer is computed using the Rapid Radiative Transfer Model (Iacono et al., 2000; Mlawer et al., 1997; Vallis et al., 2018), rather than a gray radiation scheme (e.g., Frierson, 2007), thereby permitting a water vapor feedback. Convection is represented using the simple Betts-Miller scheme (Betts, 1986; Frierson, 2007). The atmosphere is coupled to a 20 m slab ocean without heat transport. Land grid cells differ from ocean by having higher surface albedo, lower heat capacity, a finite water-holding capacity, and enhanced resistance to evaporation under dry conditions. The surface albedo for the ocean is 0.25 and for the land is 0.33. These values are higher than typical land and ocean albedo values to produce a reasonable planetary albedo in the absence of cloud radiative effects. The prescribed land heat capacity is 1/10 that of the ocean slab, equivalent to a 2 m mixed-layer ocean. Note that this land heat capacity is larger than that of modern land surfaces, but is used to simulate a realistic mean-state climate (Vallis et al., 2018). Soil moisture follows a bucket hydrology scheme (e.g., Manabe, 1969) with a capacity of 150 mm per grid cell and initial value of 100 mm. When the bucket is less than three-quarters full, evaporative resistance increases linearly with dryness; above this threshold, evaporation proceeds as over open water. Excess water is treated as runoff and returned to the ocean. In practice, the water budget remains closed because the ocean is an unlimited moisture

source, and its physics in this model are unaffected by runoff. Because these configurations lack a river routing scheme, runoff is simply discarded. Land and ocean aerodynamic roughness are set equal (0.2 mm). Snow, sea ice, and soil-moisture effects on albedo are not represented, so surface-albedo feedbacks are absent. Unless otherwise noted above, our model setup follows Isca's default template for the MiMA case of Jucker and Gerber (2017).

2.2. Experiments

We conduct 16 simulations spanning 8 continental configurations. Following Laguë et al. (2023), we first construct 6 configurations that contain 50% land and 50% ocean globally. These configurations are defined as follows: land concentrated between 30°S and 30°N ("Tropics"); land confined to high latitudes between 30° and 90° in both hemispheres ("Polar"); land restricted to the eastern hemisphere between 0°E and 180°E ("East"); land located in the Northern Hemisphere between 0° and 90°N ("North"); land distributed in two zonal bands between 180°W and 180°E at selected latitudes ("Zonal"); and land distributed in two meridional bands between 90°S and 90°N at selected longitudes ("Meridional"). We also perform an "Aquaplanet" configuration that is devoid of land and a "Realistic" configuration that closely matches today's continental geometry. For the Aquaplanet configuration, the surface albedo is set to 0.29 to match the global-mean albedo of the 50% land-ocean simulations. All simulations have no orography. For each configuration, we perform a control simulation with atmospheric CO_2 fixed at 300 ppmv, and a perturbed simulation with doubled CO_2 ($2 \times CO_2 = 600$ ppmv), branched from the control. Each simulation is integrated for 60 years. The final 50 years of each simulation are used to estimate the climate state for each continental configuration. Figure 1 shows the spatial distribution of land for each configuration (gray hatching).

3. Impact of Continental Configuration on the Climate Response

3.1. Changes in Near-Surface Air Temperature

We begin by examining changes in near-surface air temperature (δT_s). Figure 1 shows the spatial patterns of δT_s for each continental configuration in response to $2 \times CO_2$. The configurations exhibit a range of global-mean warming responses. The Aquaplanet configuration (Figure 1a) warms by $\delta \bar{T}_s = 2.9$ K (Table 1), where the overbar denotes the global mean. The Tropics land configuration (Figure 1b) exhibits the smallest global-mean warming, with $\delta \bar{T}_s = 2.4$ K. In contrast, the Polar land configuration (Figure 1c) shows stronger warming than the Aquaplanet configuration, with $\delta \bar{T}_s = 3.1$ K. Interestingly, the Realistic land configuration (Figure 1h), characterized by greater ocean coverage than the idealized land configurations but less than the Aquaplanet configuration, exhibits the largest global-mean warming, $\delta \bar{T}_s = 3.3$ K. All remaining continental configurations display comparable global-mean warming of approximately $\delta \bar{T}_s = 2.5 - 2.7$ K (Figures 1d–1f; Table 1).

A robust feature of climate change is the amplification of warming over land relative to the ocean (e.g., Byrne & O'Gorman, 2013; Dong et al., 2009; Joshi et al., 2008; Manabe et al., 1991; Stouffer & Manabe, 1999). Consistent with this behavior, land generally warms more than the ocean across the continental configurations (Figure 1). In the Tropics and Zonal land configurations, however, land and ocean warm by nearly the same amount (Figures 1b–1f), whereas in the Polar and North land configurations, where land is primarily located at high latitudes, land warming exceeds ocean warming (Figures 1c–1e). Similar behavior is seen when land extends meridionally from pole to pole but lies zonally adjacent to the ocean, producing a pronounced land-ocean warming contrast (Figures 1d–1g). Polar amplification, which is present even in the Aquaplanet configuration (Figure 1a), likely contributes to the enhanced warming over land when land is concentrated at high latitudes (compare Figures 1a and 1c). In the Realistic land configuration, land warming is strongly amplified (Figure 1h) and exhibits a pattern that reflects a combination of the Meridional and Polar land configurations (see Figures 1c and 1g). Some spatial variability in δT_s persists even without zonal asymmetries, likely due to mixed-layer and soil-atmosphere coupling.

3.2. Mechanisms for Near-Surface Warming

To investigate the processes controlling $\delta \bar{T}_s$, we employ a standard global energy balance model (Gregory et al., 2004; Gregory & Forster, 2008; Raper et al., 2002):

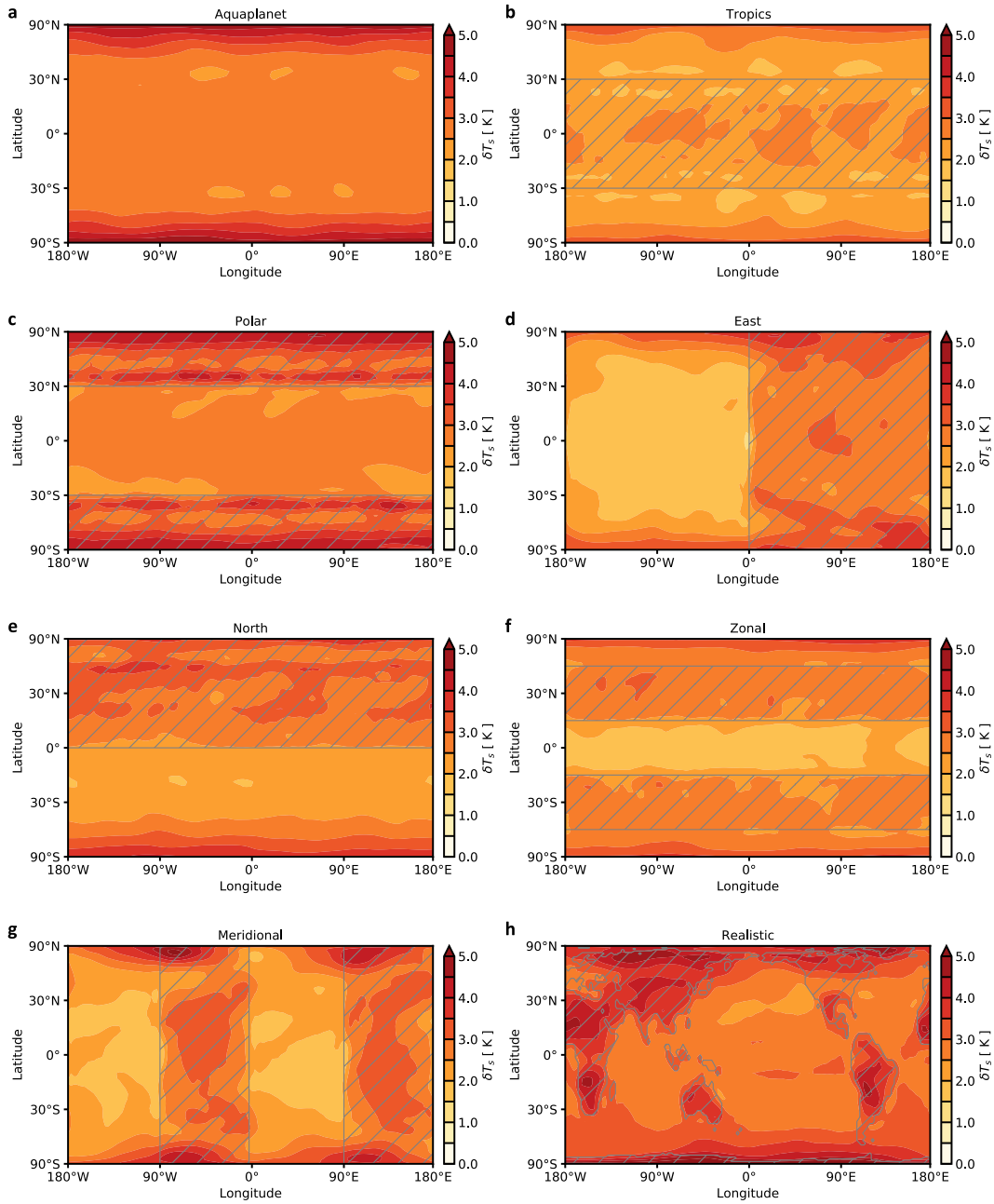

Figure 1. Continental configuration and near-surface air temperature changes. Near-surface air temperature change (δT_s) under 2 × CO_2 forcing for the (a) Aquaplanet, (b) Tropics, (c) Polar, (d) East, (e) North, (f) Zonal, (g) Meridional, and (h) Realistic land configurations. Gray hatching denotes land regions. Each land configuration contains 50% land and 50% ocean globally except for the Aquaplanet and Realistic land configurations.

$$\bar{N} = \bar{F} + \bar{\lambda}\delta\bar{T}_s, \tag{1}$$

where $\bar{N}$ is the global-mean energy imbalance (W m^{-2}), $\bar{F}$ is the global-mean effective radiative forcing (W m^{-2}), and $\bar{\lambda}$ is the global-mean radiative feedback parameter (W m^{-2} K^{-1}). In this zero-layer energy balance framework, $\bar{\lambda}$ governs the equilibrium response of $\delta\bar{T}_s$ to $\bar{F}$, representing the efficiency with which the climate system radiates energy at the top-of-atmosphere per degree of global warming. At equilibrium, $\bar{N} = 0$, which gives

Table 1
Continental Configuration and Equilibrium Climate Sensitivity

Land configuration	ECS $\equiv \delta \bar{T}_s$ K	$\bar{\mathcal{F}}$ W m^{-2}	$\bar{\lambda}$ W m^{-2} K^{-1}	$\bar{\lambda}_{\mathrm{pl}}$ W m^{-2} K^{-1}	$\bar{\lambda}_{\mathrm{wv+lr}}$ W m^{-2} K^{-1}
Aquaplanet	2.9	4.4	−1.5	−3.8	2.3
Tropics	2.4	3.6	−1.5	−3.8	2.3
Polar	3.1	3.7	−1.2	−3.9	2.7
East	2.5	3.5	−1.4	−3.8	2.4
North	2.7	3.8	−1.4	−3.8	2.4
Zonal	2.6	3.9	−1.5	−3.8	2.3
Meridional	2.6	3.7	−1.4	−3.8	2.4
Realistic	3.3	3.6	−1.1	−3.9	2.8

Note. The equilibrium climate sensitivity (ECS), defined as the equilibrium global-mean near-surface air temperature change ($\delta \bar{T}_s$) following a doubling of CO_2, for each land configuration. The global-mean radiative forcing ($\bar{\mathcal{F}}$) and global-mean net radiative feedback ($\bar{\lambda}$) are shown in the next two columns. The $\bar{\lambda}$ term is further partitioned into a component due to the Planck feedback ($\bar{\lambda}_{\mathrm{pl}}$) and a component due to the combined water vapor and lapse rate feedbacks ($\bar{\lambda}_{\mathrm{wv+lr}}$). Each land configuration contains 50% land and 50% ocean globally except for the Aquaplanet and Realistic land configurations.

$$\mathrm{ECS} \equiv \delta \bar{T}_s = -\frac{\bar{\mathcal{F}}}{\bar{\lambda}}. \tag{2}$$

where ECS is the equilibrium climate sensitivity, defined as the equilibrium global-mean near-surface air temperature change in response to 2 × CO_2.

Table 1 shows the values of ECS, $\bar{\mathcal{F}}$, and $\bar{\lambda}$ for each continental configuration. $\bar{\mathcal{F}}$ and $\bar{\lambda}$ are estimated as the y-intercept and slope, respectively, of the linear relationship between $\delta \bar{T}_s$ and $\bar{N}$ over the first 10 years of the 2 × CO_2 simulation. This regression period is shorter than that used in other studies (e.g., Gregory et al., 2004), reflecting the faster equilibration timescale of our simulations. The configurations with land exhibit similar values of $\bar{\mathcal{F}}$, ranging from 3.5 to 3.9 W m^{-2}, whereas $\bar{\lambda}$ has a larger fractional variation. Note that the Aquaplanet configuration has a larger value of $\bar{\mathcal{F}} = 4.4$ W m^{-2}. The Tropics land configuration, which has the smallest ECS, has the most negative $\bar{\lambda}$, indicating strong radiative damping (Table 1). Conversely, the Polar land configuration, which exhibits a large ECS, has a small negative $\bar{\lambda}$, indicating weak radiative damping (Table 1). Notably, the Realistic land configuration has the largest ECS and the least negative $\bar{\lambda}$, even compared with the Aquaplanet simulation, which has more extensive ocean coverage and thus a greater supply of moisture (Table 1).

Typically, $\bar{\lambda}$ is partitioned into individual feedbacks (e.g., water vapor, lapse rate) using radiative kernels (e.g., Shell et al., 2008; Soden et al., 2008). Kernels for the RRTM scheme in Isca exist (e.g., Chung & Feldl, 2024) but depend on the base climate state, which varies across continental configurations (Laguë et al., 2023), and applying them consistently is computationally prohibitive. Since these simulations exclude cloud and surface albedo feedbacks, variations in $\bar{\lambda}$ arise solely from the Planck, water vapor, and lapse rate feedbacks. We therefore partition $\bar{\lambda}$ into the Planck component ($\bar{\lambda}_{\mathrm{pl}}$) and the combined water vapor plus lapse rate component ($\bar{\lambda}_{\mathrm{wv+lr}}$), which covary strongly (Held & Shell, 2012; Po-Chedley et al., 2018). The term $\bar{\lambda}_{\mathrm{pl}}$ is estimated via the Stefan-Boltzmann law (e.g., Bony et al., 2006; Cronin & Dutta, 2023):

$$\bar{\lambda}_{\mathrm{pl}} = -4\sigma \bar{T}_e^3, \tag{3}$$

where σ is the Stefan-Bolztmann constant and $\bar{T}_e$ is the global-mean effective emission temperature, estimated as

$$\bar{T}_e = \left(\frac{\bar{F}_0}{\sigma}\right)^{1/4}, \tag{4}$$

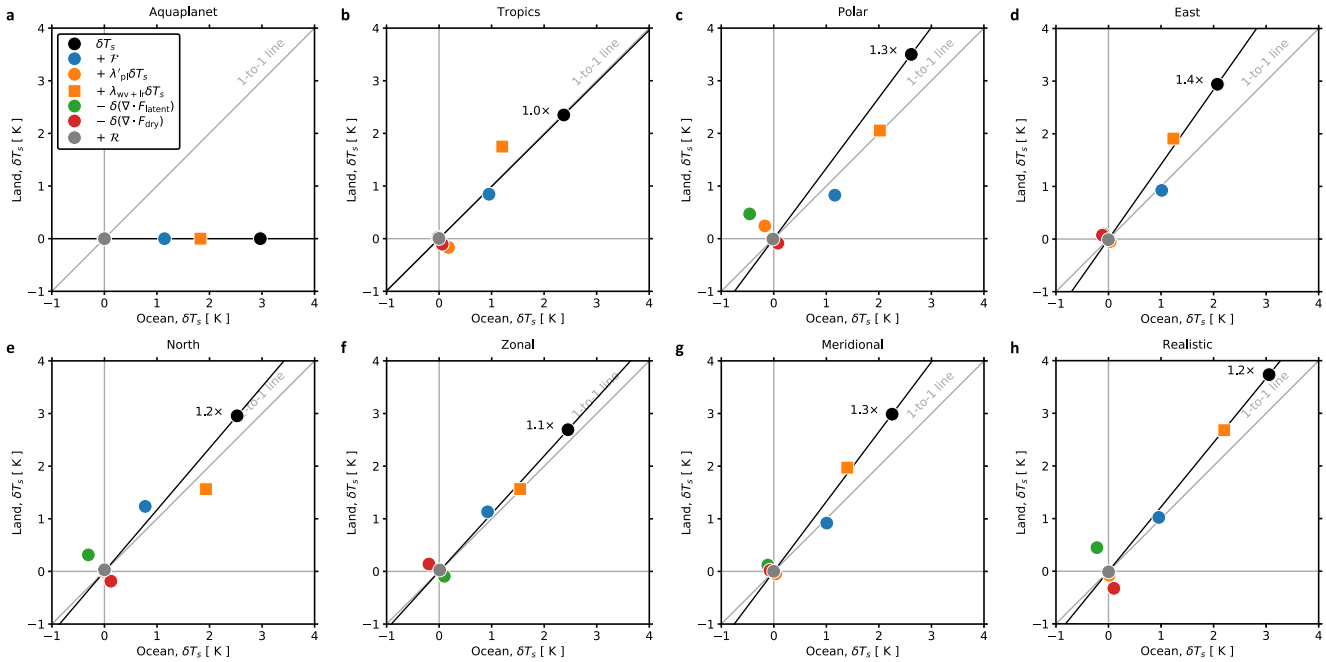

Figure 2. Mechanisms for land–ocean warming contrasts. Scatter plot showing the change in near-surface air temperature (δT_s) under 2 × CO_2 over the ocean (*x*-axis) versus over the land (*y*-axis) for the (a) Aquaplanet, (b) Tropics, (c) Polar, (d) East, (e) North, (f) Zonal, (g) Meridional, and (h) Realistic land configurations. Each colored symbol represents a specific mechanism from Equation 5. The ratio of land warming to ocean warming is indicated by the black text adjacent to the black dot. Each land configuration contains 50% land and 50% ocean globally except for the Aquaplanet and Realistic land configurations.

with $\bar{F}_0$ representing the global-mean outgoing longwave radiation at the top-of-atmosphere in the control simulation (i.e., atmospheric CO_2 of 300 ppm). The value of $\bar{\lambda}_{\rm wv+lr}$ for each simulation is then calculated as the difference between the total $\bar{\lambda}$ (estimated via regression) and $\bar{\lambda}_{\rm pl}$.

In the Tropics land configuration, where $\bar{\lambda}$ is most negative, $\bar{\lambda}_{\rm wv+lr}$ is less positive. This likely reflects the fact that land in the tropics reduces evaporation compared with the ocean in the base climate state, which limits atmospheric water vapor and weakens the water vapor feedback. Conversely, in the Polar land configuration, where $\bar{\lambda}$ is less negative, $\bar{\lambda}_{\rm wv+lr}$ is more positive. This is likely due to a strong water vapor base state maintained by enhanced evaporation over tropical oceans. In the Realistic land configuration, $\bar{\lambda}$ is the least negative, likely because of a strongly positive water vapor feedback associated with limited tropical land area and a less negative lapse-rate feedback over extratropical land surfaces.

To understand the differences in land-ocean warming contrasts, we examine changes in the local atmospheric energy budget (Crook et al., 2011; Feldl et al., 2017; Goosse et al., 2018; Hahn et al., 2021; Pithan & Mauritsen, 2014) and decompose δT_s into contributions from $\mathcal{F}$, λ, and changes in the atmospheric energy flux convergence. In these equilibrium slab ocean model simulations, there is no change in the net surface energy flux. Using $\bar{\lambda}_{\rm pl}$ and assuming a balanced atmospheric energy budget, the local δT_s can thus be expressed as

$$\delta T_s = -\frac{1}{\bar{\lambda}_{\rm pl}}\left(\mathcal{F} + \lambda'_{\rm pl}\delta T_s + \lambda_{\rm wv+lr}\delta T_s - \delta(\nabla \cdot F_{\rm dry}) - \delta(\nabla \cdot F_{\rm latent}) + \varepsilon\right), \tag{5}$$

where $\lambda'_{\rm pl} = \lambda_{\rm pl} - \bar{\lambda}_{\rm pl}$, $\delta(\nabla \cdot F_{\rm dry})$ is the change in the dry-static energy flux convergence, $\delta(\nabla \cdot F_{\rm latent})$ is the change in the latent energy flux convergence, and ε is small residual term accounting for nonlinearties in the approximation of $\mathcal{F}$ and λ. Note that $\mathcal{F}$ and λ are computed as the *y*-intercept and slope, respectively, of the relationship between δT_s and N over the first 10 years, calculated separately for the global average land and ocean domains. We further partition λ into $\lambda_{\rm pl}$ and $\lambda_{\rm wv+lr}$ following the procedure described above but over the global average land and ocean domains. The term $\delta(\nabla \cdot F_{\rm latent})$ is calculated from the change in evaporation minus

precipitation times the latent heat of vapourization, while $\delta(\nabla \cdot F_{\text{dry}})$ is calculated as the difference between the change in net top-of-atmosphere energy flux and $\delta(\nabla \cdot F_{\text{latent}})$.

Figure 2 shows δT_s averaged over the ocean (x-axis) versus δT_s averaged over the land (y-axis) as black dots, along with the contributions of each term in Equation 5, shown as colored dots, for each continental configuration. In the Tropics land configuration, land and ocean temperatures increase by the same amount, indicating no amplification of warming over land (black dot, Figure 2b). All other continental configurations exhibit some degree of land amplification, with the largest land-ocean warming contrast occurring in the East land configuration (black dot, Figure 2d) and the smallest in the Zonal land configuration (black dot, Figure 2f), corresponding to amplification factors of 1.4× and 1.1 ×, respectively. The Realistic land configuration also exhibits a moderate land–ocean warming contrast, with an amplification factor of 1.2× (Figure 2h).

Although most continental configurations exhibit amplified land warming, the mechanisms driving this amplification differ. In the East and Meridional land configurations, which have the largest amplification factors, the combined water vapor and lapse-rate feedback accounts for nearly all of the land-ocean warming contrast (orange squares; Figures 2d and 2g), consistent with previous studies examining land warming in more realistic simulations (e.g., Sejas et al., 2014). Over land, the lapse-rate feedback is weaker (less negative) because limited moisture keeps the temperature profile closer to the dry adiabat, reducing upper-tropospheric warming and radiative damping compared to the moist-adiabatic ocean (Byrne & O'Gorman, 2013; Joshi et al., 2008). In contrast, in the Polar and North land configurations, land-ocean warming amplification is driven primarily by increased latent energy flux convergence (green dots; Figures 2c–2e), a well-known consequence of global warming (Bonan et al., 2023; Held & Soden, 2006; Siler et al., 2018). This enhanced flux convergence likely reflects the polar placement of land and the associated increase in meridional latent energy transport that also contributes to polar amplification (Armour et al., 2019; Bonan et al., 2018; Merlis & Henry, 2018). In the Polar land configuration, the Planck feedback further amplifies land warming because colder land in the control state reduces radiative emission, weakening stabilizing damping (orange dot; Figure 2c). In the Tropics land configuration, which shows little-to-no land-ocean warming contrast, the combined water vapor and lapse-rate feedback is largely offset by the Planck response, yielding minimal net amplification (orange symbols, Figure 2b). Land-ocean warming in the Realistic land configuration reflects a combination of the Polar and Meridional land configurations, with both increased latent energy flux convergence and a weaker lapse-rate feedback over land contributing (green dot and orange square, Figure 1h).

3.3. Changes in Near-Surface Relative Humidity

Another prominent aspect of the land response to climate change is a decline in near-surface relative humidity ($\mathcal{H}$; Byrne & O'Gorman, 2016; Fu & Feng, 2014; O'Gorman & Muller, 2010; Laîné et al., 2014). Figure 3 shows the fractional change in near-surface relative humidity ($\delta\mathcal{H}/\mathcal{H}$), normalized by δT_s, for each continental configuration. Across all configurations, land generally exhibits a decline in $\mathcal{H}$, although substantial spatial variability exists and some regions experience increases. In the Tropics land configuration, $\mathcal{H}$ decreases strongly in the continental interior (20°S–20°N) but increases along the poleward edges of the continent (20°–30°N/S; Figure 3b). The Polar land configuration shows drying primarily confined to subtropical zonal bands (30°–45°N/S; Figure 3c). In the East and Meridional land configurations, where land extends meridionally from pole to pole but remains zonally adjacent to the ocean, $\mathcal{H}$ increases along the western continental margins in the tropics (20°S–20°N), with weaker decreases elsewhere (Figures 3d and 3g). The North land configuration exhibits the strongest drying, with pronounced reductions in $\mathcal{H}$ across the extratropical continental interior (20°–60°N) and localized increases near coastal regions (0°–10°N; Figure 3e). The Zonal land configuration shows a relatively uniform decline in $\mathcal{H}$ (Figure 3f). Finally, the Realistic land configuration exhibits widespread drying over subtropical land areas, accompanied by moderate increases in $\mathcal{H}$ over tropical regions, including equatorial Africa, South America, southern India, and Indonesia (Figure 3h).

3.4. Mechanisms for Near-Surface Relative Humidity Changes Over Land

To understand the mechanisms contributing to $\delta\mathcal{H}$, we follow Byrne and O'Gorman (2016) by using a conceptual box model that approximates near-surface land specific humidity (q_l) as a function of atmospheric moisture transport between land and ocean, and land surface evaporation. We begin by defining near-surface land relative humidity, $\mathcal{H}_l$, as

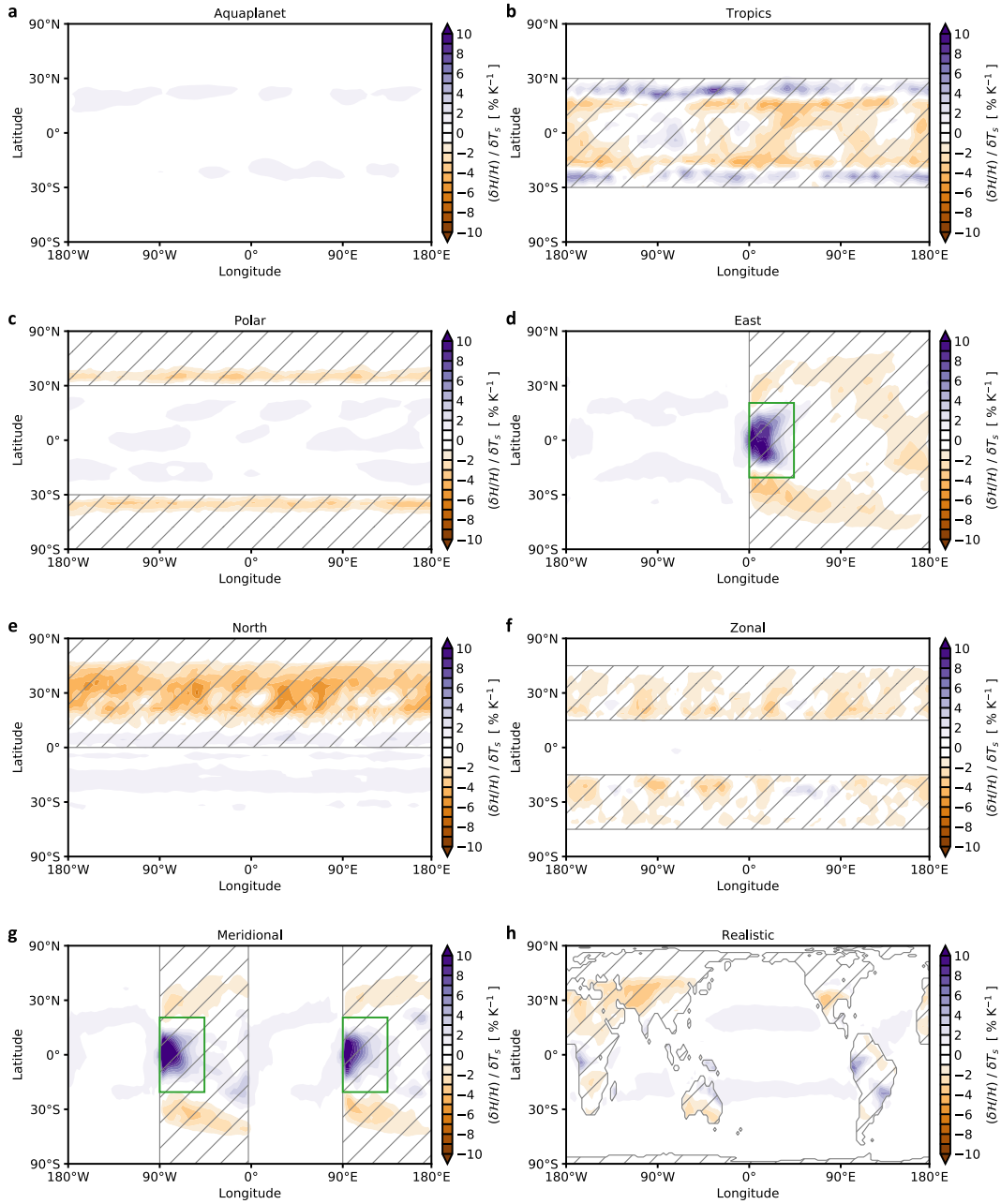

Figure 3. Continental configuration and near-surface relative humidity changes. The fractional change in near-surface relative humidity ($\delta\mathcal{H}/\mathcal{H}$) normalized by change in near-surface air temperature (δT_s) under 2 × CO_2 forcing for the (a) Aquaplanet, (b) Tropics, (c) Polar, (d) East, (e) North, (f) Zonal, (g) Meridional, and (h) Realistic land configurations. Gray hatching denotes land regions. Each land configuration contains 50% land and 50% ocean globally except for the Aquaplanet and Realistic land configurations. The green boxes in panels (d, g) denote the regional domains used in Figure 4.

$$\mathcal{H}_l = \frac{q_l}{q_l^*}, \tag{6}$$

where q_l^* is the near-surface land specific humidity at saturation. The fractional change in $\mathcal{H}_l$ can be expressed in terms of the fractional changes of two components:

$$\frac{\delta \mathcal{H}_l}{\mathcal{H}_l} \approx \frac{\delta q_l}{q_l} - \frac{\delta q_l^*}{q_l^*}. \tag{7}$$

The term $\delta q_l^*/q_l^*$ can be expressed as $\alpha_l \, \delta T_l$, so that, when normalized by δT_l, Equation 7 becomes

$$\frac{1}{\delta T_l}\frac{\delta \mathcal{H}_l}{\mathcal{H}_l} \approx \frac{1}{\delta T_l}\frac{\delta q_l}{q_l} - \alpha_l, \tag{8}$$

where α_l is the Clausius-Clapeyron scaling factor, defined as

$$\alpha_l = \frac{L_v}{R_v T_l^2}, \tag{9}$$

with L_v denoting the latent heat of vapourization, R_v the gas constant for water vapor, and T_l the near-surface air temperature over land in the control simulation. Equation 8 indicates that fractional changes in $\mathcal{H}_l$ can be largely attributed to fractional changes in q_l, since α_l varies little when averaged globally over land (shown below). To further investigate the factors contributing to δq_l, we follow Byrne and O'Gorman (2016) and approximate q_l as

$$q_l \approx \gamma q_o + \beta E_l, \tag{10}$$

where q_o is the near-surface ocean specific humidity, γ is a coupling coefficient representing the influence of atmospheric moisture transport from ocean to land, E_l is the local land surface evaporation, and β is a coupling coefficient describing the sensitivity of local evaporation to near-surface land humidity. Linearizing Equation 10 gives

$$\delta q_l \approx \underbrace{\gamma \delta q_o}_{\text{(A)}} + \underbrace{\delta\gamma q_o}_{\text{(B)}} + \underbrace{\beta \delta E_l}_{\text{(C)}} + \underbrace{\delta\beta E_l}_{\text{(D)}}, \tag{11}$$

where (A-B) represent changes in q_l due to atmospheric moisture transport from the ocean, either from (A) increases in ocean humidity (δq_o) or (B) changes in mixing efficiency ($\delta\gamma$), and (C-D) represent changes in q_l due to land surface evaporation, either from (C) changes in surface evaporation (δE_l) or (D) changes in the coupling coefficient relating local evaporation to near-surface land humidity ($\delta\beta$). Together, Equations 8 and 11 provide a framework for attributing $\delta \mathcal{H}_l$ to distinct mechanisms. We calibrate the conceptual box model for each continental configuration using multiple linear regression, with global-mean ocean specific humidity (q_o) and global-mean land evaporation (E_l) as predictors of q_l. This calibration uses 50-year annual-mean time series from both the control and 2× CO_2 simulations, allowing us to estimate γ and β for each climate state via Equation 10. The multiple linear regression model explains over 90% of the interannual variance in both the equilibrated control and perturbed simulations (not shown).

Figure 4 shows $(\delta\mathcal{H}/\mathcal{H})/\delta T_s$ over the global-mean land surface for each continental configuration (Figure 4a). The largest global-mean declines occur when land is located mainly in the extratropics, with the Polar, North, and Zonal land configurations exhibiting the strongest decreases. In contrast, the Tropics and East land configurations show smaller declines, the Meridional land configuration exhibits a slight increase, and the Realistic land configuration shows a moderate decline.

Differences in $(\delta\mathcal{H}/\mathcal{H})/\delta T_s$ across the continental configurations are largely driven by variations in δq_l, as all configurations display similar values of α_l, close to the canonical value of 7% K^{-1} (purple dashed line, Figure 4b). For instance, the North land configuration shows a smaller increase in q_l compared with the East or Tropics land configurations (Figure 4b), resulting in a larger decline in $(\delta\mathcal{H}/\mathcal{H})/\delta T_s$. In the North land configuration, the relatively weak increase in q_l is linked to smaller increases in oceanic moisture transport compared to most of the other configurations (blue bars, Figure 4c). By contrast, the increase in q_l in the East land configuration is primarily due to a large increase in land evaporation (orange bar, Figure 4c). Further partitioning of these terms into contributions from changes in atmospheric mixing efficiency versus boundary-layer properties reveals additional configuration-specific differences. For example, in the North and Polar land configurations, limited zonal

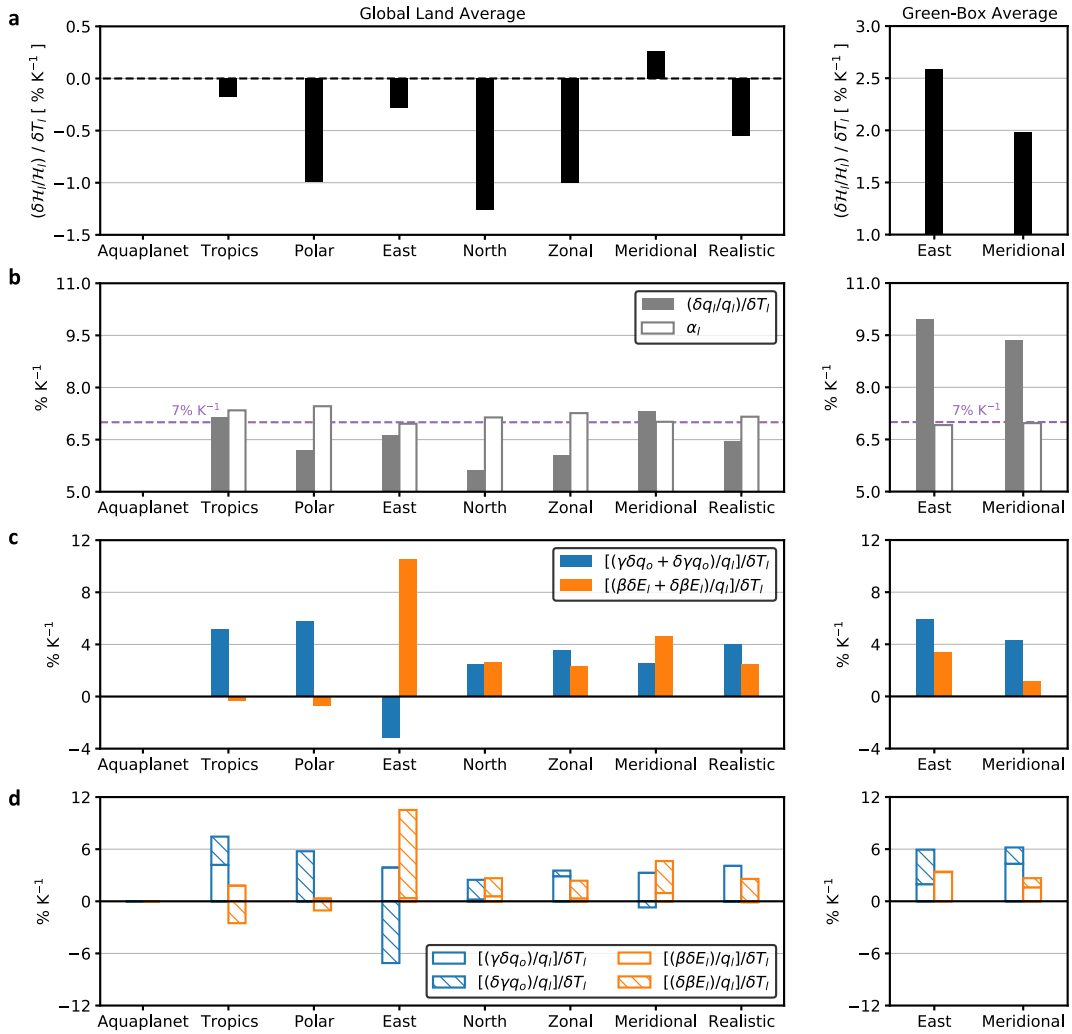

Figure 4. Mechanisms for relative humidity changes over land. (a) The fractional change in near-surface relative humidity over land ($\delta\mathcal{H}_l/\mathcal{H}_l$) normalized by change in near-surface air temperature over land (δT_l). (b) Decomposition of $(\delta\mathcal{H}_l/\mathcal{H}_l)/\delta T_l$ into contributions from fractional increases in near-surface land specific humidity $\left(\delta q_l/q_l\right)/\delta T_l$ and saturation land component (α_l). The purple dashed line denotes the canonical value of $\alpha = 7\%$ K^{-1}. Panel (c) As in panel (b), but the filled Gy bar decomposed into contributions from the oceanic moisture transport term (blue bar) and the land surface evaporation term (orange bar). (d) Further decomposition of the blue and orange bars in panel (c) into contributions from changes in ocean specific humidity (δq_o, blue open bar), changes in the atmospheric mixing efficiency ($\delta\gamma$, blue hatched bar), changes in land surface evaporation (δE_l, orange open bar), and changes in the coupling coefficient relating evaporation to land specific humidity ($\delta\beta$, orange hatched bar). The left panels show the global land average and the right panels show the green box average shown in Figures 3d and 3g.

moisture transport in the control climate—which is typically larger than meridional moisture transport—results in essentially no oceanic moisture transport via atmospheric mixing (i.e., $\gamma = 0$). Consequently, increases in oceanic moisture transport under warming are instead tied to $\delta\gamma$ (blue hatched bars, Figure 4d). The absence of atmospheric mixing with ocean regions in the control climate for these configurations also limits the increase in δq_l compared with other configurations, resulting in stronger drying. The Realistic land configuration exhibits moderate drying of global land that is consistent with a combination of the Meridional and Polar land configurations (Figures 4a–4d). More generally, these results suggest that, under warming, continental configuration shapes both the spatial pattern and magnitude of $\delta\mathcal{H}$, though the precise mechanisms are distinct.

The conceptual box model can also be used to explore regional features, such as the pronounced increase in $(\delta\mathcal{H}/\mathcal{H})/\delta T_s$ along the western tropical margins of the continents in the East and Meridional land configurations (green boxes in Figures 3c and 3e), which is also present, though weaker, in the Realistic land configuration

(Figure 3h). We calibrate the model using the same procedure described above, but restricted to the green-box domains. Within these domains, $\mathcal{H}_l$ increases by 2.6% K^{-1} and 2% K^{-1} in the East and Meridional land configurations, respectively. This increase is linked to a substantial increase in δq_l, which is driven primarily by the oceanic moisture transport term, with a smaller contribution from the evaporation term (Figures 4b and 4c). Notably, the influence of oceanic moisture transport on δq_l reflects changes in atmospheric mixing efficiency (i.e., $\delta\gamma$) with some contribution from δq_o (compare blue bars, Figure 4d). These results suggest that, under warming, meridionally oriented land adjacent to the ocean enhances $\mathcal{H}_l$ along the tropical western flanks of continents primarily by modifying the transport of humidity from adjacent ocean. We note that the local low-level zonal winds strengthen (not shown), perhaps because these regions also exhibit strong local land-ocean warming contrasts (Figures 1d–1g), suggesting that enhanced land warming may drive a stronger near-surface pressure gradient and shallow onshore flow, thereby increasing γ.

4. Discussion and Conclusions

The distribution of continents fundamentally shapes Earth's climate, yet its role in the climate response to increased greenhouse-gas concentrations remains poorly understood. In this study, we use an idealized GCM to explore how different continental configurations affect the climate response to elevated greenhouse gases. Our results show that when land is concentrated in the tropics, equilibrium climate sensitivity is lower, land-ocean warming contrasts are minimal, and global-mean land relative humidity declines only slightly. By contrast, when land is concentrated at high latitudes, equilibrium climate sensitivity increases, land-ocean warming contrasts become pronounced, and global-mean land relative humidity declines substantially. The largest land-ocean warming contrasts arise when land is located in the polar regions or extends in a continuous meridional band zonally adjacent to the ocean. Interestingly, simulations with a realistic land distribution exhibit the largest ECS, even compared to an aquaplanet simulation with greater ocean coverage.

While these results provide a first-order picture, several caveats should be noted. Most importantly, these simulations do not include clouds, which remain one of the most uncertain aspects of climate change (e.g., Zelinka et al., 2017). Similarly, we do not account for changes in ocean circulation, which are likely to differ substantially under these continental configurations and could lead to different patterns of ocean heat transport and base climate states. For example, Ladant et al. (2020) showed that when land is concentrated into a single large mass, the general ocean circulation simulated by a climate model becomes much weaker. Another limitation arises from the relatively simple land-surface model used in this study. We assumed a uniform "bucket depth," effectively implying the same soil type everywhere. In reality, such drastically different continental configurations would likely imply different soil properties, manifesting as variations in bucket depth and in the capacity to redistribute moisture across the land surface (e.g., via rivers and lakes). More sophisticated land surface models that include active vegetation (e.g., Bonan et al., 2024; Fisher & Koven, 2020) could also substantially alter these results. Each of these caveats could be addressed in future work.

Overall, despite their idealized nature, these simulations provide insight into modern-day climate change. For example, observations and climate model simulations show that India, East Africa, and parts of Australia have experienced, or are projected to experience, increases in near-surface relative humidity, whereas most other land regions exhibit decreases (e.g., Byrne & O'Gorman, 2016; Siler et al., 2023; Vicente-Serrano et al., 2018). Our results suggest that these increases may be linked to changes in atmospheric mixing between the ocean and land driven by continental geometry. In the Realistic land configuration, these land areas exhibit a moderate increase in near-surface relative humidity under warming, a feature that is even more pronounced in tropical regions of idealized continents that extend meridionally in a manner similar to modern-day Earth. This contrasts with previous work that attributed the increase in near-surface relative humidity over India specifically to enhanced local evaporation associated with increased irrigation (Mishra et al., 2020). More broadly, these results offer a first-order perspective on how continental configuration can modulate Earth's climate response to external forcing, with potential implications for interpreting paleogeographic climate records. Future studies should consider the impact of more realistic continental configurations (e.g., Li et al., 2022) on the climate response to greenhouse-gas forcing.

Conflict of Interest

The authors declare no conflicts of interest relevant to this study.

Data Availability Statement

Model output from this study can be found at Zenodo (Bonan, 2026). Information about the Isca framework, including the MiMA configuration, is available here: http://www.exeter.ac.uk/isca.

Acknowledgments
The authors acknowledge high-performance computing support from a National Center for Atmospheric Research (NCAR) Small Exploratory Computing Grant, using the Cheyenne and Derecho systems provided by NCAR's Computational and Information Systems Laboratory, which is supported by the National Science Foundation. D.B.B. was supported by a Cooperative Institute for Climate, Ocean, and Ecosystem Studies (CICOES) Postdoctoral Fellowship. This publication is partially funded by CICOES under NOAA Cooperative Agreement NA20OAR4320271, Contribution No. 2025-1494. M.M.L.'s contributions were partially supported by the Natural Sciences and Engineering Research Council of Canada's Discovery Grant Program, award number RGPIN-2025-04261. W.R.B. was supported by the National Science Foundation under Grant 2412755. D.B.B and M.M.L thank the Advanced Climate Dynamics Course (ACDC) for inspiring some of this research. The authors thank two anonymous reviewers and the Editor for their careful and constructive feedback, which improved the analysis in this manuscript.

References

Armour, K. C., Siler, N., Donohoe, A., & Roe, G. H. (2019). Meridional atmospheric heat transport constrained by energetics and mediated by large-scale diffusion. *Journal of Climate*, *32*(12), 3655–3680. https://doi.org/10.1175/jcli-d-18-0563.1

Barker, P., & Burrell, J. (1977). The opening of drake passage. *Marine Geology*, *25*(1–3), 15–34. https://doi.org/10.1016/0025-3227(77)90045-7

Betts, A. K. (1986). A new convective adjustment scheme. Part I: Observational and theoretical basis. *Quarterly Journal of the Royal Meteorological Society*, *112*(473), 677–691. https://doi.org/10.1256/smsqj.47306

Bonan, D. B. (2026). Impact of continental configuration on the climate response to greenhouse-gas forcing in an idealized GCM [Dataset]. *Zenodo*. https://doi.org/10.5281/zenodo.18248438

Bonan, D. B., Armour, K. C., Roe, G. H., Siler, N., & Feldl, N. (2018). Sources of uncertainty in the meridional pattern of climate change. *Geophysical Research Letters*, *45*(17), 9131–9140. https://doi.org/10.1029/2018gl079429

Bonan, D. B., Siler, N., Roe, G. H., & Armour, K. C. (2023). Energetic constraints on the pattern of changes to the hydrological cycle under global warming. *Journal of Climate*, *36*(10), 3499–3522. https://doi.org/10.1175/jcli-d-22-0337.1

Bonan, G. B., Lucier, O., Coen, D. R., Foster, A. C., Shuman, J. K., Laguë, M. M., et al. (2024). Reimagining Earth in the Earth system. *Journal of Advances in Modeling Earth Systems*, *16*(8), e2023MS004017. https://doi.org/10.1029/2023ms004017

Bony, S., Colman, R., Kattsov, V. M., Allan, R. P., Bretherton, C. S., Dufresne, J.-L., et al. (2006). How well do we understand and evaluate climate change feedback processes? *Journal of Climate*, *19*(15), 3445–3482. https://doi.org/10.1175/jcli3819.1

Byrne, M. P., & O'Gorman, P. A. (2013). Land–ocean warming contrast over a wide range of climates: Convective quasi-equilibrium theory and idealized simulations. *Journal of Climate*, *26*(12), 4000–4016. https://doi.org/10.1175/jcli-d-12-00262.1

Byrne, M. P., & O'Gorman, P. A. (2016). Understanding decreases in land relative humidity with global warming: Conceptual model and GCM simulations. *Journal of Climate*, *29*(24), 9045–9061. https://doi.org/10.1175/jcli-d-16-0351.1

Chung, P.-C., & Feldl, N. (2024). Sea ice loss, water vapor increases, and their interactions with atmospheric energy transport in driving seasonal polar amplification. *Journal of Climate*, *37*(8), 2713–2725. https://doi.org/10.1175/jcli-d-23-0219.1

Croll, J. (1870). Xii. on ocean-currents, part i: Ocean-currents in relation to the distribution of heat over the globe. *Philosophical Magazine and Journal of Science*, *39*(259), 81–101.

Cronin, T. W., & Dutta, I. (2023). How well do we understand the planck feedback? *Journal of Advances in Modeling Earth Systems*, *15*(7), e2023MS003729. https://doi.org/10.1029/2023ms003729

Crook, J. A., Forster, P. M., & Stuber, N. (2011). Spatial patterns of modeled climate feedback and contributions to temperature response and polar amplification. *Journal of Climate*, *24*(14), 3575–3592. https://doi.org/10.1175/2011jcli3863.1

Dong, B., Gregory, J. M., & Sutton, R. T. (2009). Understanding land–sea warming contrast in response to increasing greenhouse gases. Part I: Transient adjustment. *Journal of Climate*, *22*(11), 3079–3097. https://doi.org/10.1175/2009jcli2652.1

Feldl, N., Bordoni, S., & Merlis, T. M. (2017). Coupled high-latitude climate feedbacks and their impact on atmospheric heat transport. *Journal of Climate*, *30*(1), 189–201. https://doi.org/10.1175/jcli-d-16-0324.1

Ferreira, D., Cessi, P., Coxall, H. K., De Boer, A., Dijkstra, H. A., Drijfhout, S. S., et al. (2018). Atlantic-Pacific asymmetry in deep water formation. *Annual Review of Earth and Planetary Sciences*, *46*(1), 327–352. https://doi.org/10.1146/annurev-earth-082517-010045

Fisher, R. A., & Koven, C. D. (2020). Perspectives on the future of land surface models and the challenges of representing complex terrestrial systems. *Journal of Advances in Modeling Earth Systems*, *12*(4), e2018MS001453. https://doi.org/10.1029/2018ms001453

Frierson, D. M. (2007). The dynamics of idealized convection schemes and their effect on the zonally averaged tropical circulation. *Journal of the Atmospheric Sciences*, *64*(6), 1959–1976. https://doi.org/10.1175/jas3935.1

Fu, Q., & Feng, S. (2014). Responses of terrestrial aridity to global warming. *Journal of Geophysical Research: Atmospheres*, *119*(13), 7863–7875. https://doi.org/10.1002/2014jd021608

Goosse, H., Kay, J. E., Armour, K. C., Bodas-Salcedo, A., Chepfer, H., Docquier, D., et al. (2018). Quantifying climate feedbacks in polar regions. *Nature Communications*, *9*(1), 1919. https://doi.org/10.1038/s41467-018-04173-0

Gregory, J. M., & Forster, P. (2008). Transient climate response estimated from radiative forcing and observed temperature change. *Journal of Geophysical Research*, *113*(D23). https://doi.org/10.1029/2008jd010405

Gregory, J. M., Ingram, W. J., Palmer, M., Jones, G. S., Stott, P., Thorpe, R., et al. (2004). A new method for diagnosing radiative forcing and climate sensitivity. *Geophysical Research Letters*, *31*(3). https://doi.org/10.1029/2003gl018747

Hahn, L. C., Armour, K. C., Zelinka, M. D., Bitz, C. M., & Donohoe, A. (2021). Contributions to polar amplification in CMIP5 and CMIP6 models. *Frontiers in Earth Science*, *9*, 710036. https://doi.org/10.3389/feart.2021.710036

Held, I. M., & Shell, K. M. (2012). Using relative humidity as a state variable in climate feedback analysis. *Journal of Climate*, *25*(8), 2578–2582. https://doi.org/10.1175/jcli-d-11-00721.1

Held, I. M., & Soden, B. J. (2006). Robust responses of the hydrological cycle to global warming. *Journal of Climate*, *19*(21), 5686–5699. https://doi.org/10.1175/jcli3990.1

Iacono, M. J., Mlawer, E. J., Clough, S. A., & Morcrette, J.-J. (2000). Impact of an improved longwave radiation model, RRTM, on the energy budget and thermodynamic properties of the NCAR community climate model, CCM3. *Journal of Geophysical Research*, *105*(D11), 14873–14890. https://doi.org/10.1029/2000jd900091

Jones, C. S., & Cessi, P. (2017). Size matters: Another reason why the Atlantic is saltier than the Pacific. *Journal of Physical Oceanography*, *47*(11), 2843–2859. https://doi.org/10.1175/jpo-d-17-0075.1

Joshi, M. M., Gregory, J. M., Webb, M. J., Sexton, D. M., & Johns, T. C. (2008). Mechanisms for the land/sea warming contrast exhibited by simulations of climate change. *Climate Dynamics*, *30*(5), 455–465. https://doi.org/10.1007/s00382-007-0306-1

Jucker, M., & Gerber, E. (2017). Untangling the annual cycle of the tropical tropopause layer with an idealized moist model. *Journal of Climate*, *30*(18), 7339–7358. https://doi.org/10.1175/jcli-d-17-0127.1

Ladant, J.-B., Poulsen, C. J., Fluteau, F., Tabor, C. R., MacLeod, K. G., Martin, E. E., et al. (2020). Paleogeographic controls on the evolution of Late Cretaceous ocean circulation. *Climate of the Past*, *16*(3), 973–1006. https://doi.org/10.5194/cp-16-973-2020

Laguë, M. M., Quetin, G. R., Ragen, S., & Boos, W. R. (2023). Continental configuration controls the base-state water vapor greenhouse effect: Lessons from half-land, half-water planets. *Climate Dynamics*, *61*(11), 5309–5330. https://doi.org/10.1007/s00382-023-06857-w

Laîné, A., Nakamura, H., Nishii, K., & Miyasaka, T. (2014). A diagnostic study of future evaporation changes projected in CMIP5 climate models. *Climate Dynamics*, *42*(9), 2745–2761. https://doi.org/10.1007/s00382-014-2087-7

Li, X., Hu, Y., Guo, J., Lan, J., Lin, Q., Bao, X., et al. (2022). A high-resolution climate simulation dataset for the past 540 million years. *Scientific Data*, *9*(1), 371. https://doi.org/10.1038/s41597-022-01490-4

Manabe, S. (1969). Climate and the ocean circulation: I. The atmospheric circulation and the hydrology of the earth's surface. *Monthly Weather Review*, *97*(11), 739–774. https://doi.org/10.1175/1520-0493(1969)097<0739:catoc>2.3.co;2

Manabe, S., Stouffer, R. J., Spelman, M. J., & Bryan, K. (1991). Transient responses of a coupled ocean–atmosphere model to gradual changes of atmospheric CO2. Part I. Annual mean response. *Journal of Climate*, *4*(8), 785–818. https://doi.org/10.1175/1520-0442(1991)004<0785:troaco>2.0.co;2

Merdith, A. S., Williams, S. E., Collins, A. S., Tetley, M. G., Mulder, J. A., Blades, M. L., et al. (2021). Extending full-plate tectonic models into deep time: Linking the Neoproterozoic and the Phanerozoic. *Earth-Science Reviews*, *214*, 103477. https://doi.org/10.1016/j.earscirev.2020.103477

Merlis, T. M., & Henry, M. (2018). Simple estimates of polar amplification in moist diffusive energy balance models. *Journal of Climate*, *31*(15), 5811–5824. https://doi.org/10.1175/jcli-d-17-0578.1

Mishra, V., Ambika, A. K., Asoka, A., Aadhar, S., Buzan, J., Kumar, R., & Huber, M. (2020). Moist heat stress extremes in India enhanced by irrigation. *Nature Geoscience*, *13*(11), 722–728. https://doi.org/10.1038/s41561-020-00650-8

Mlawer, E. J., Taubman, S. J., Brown, P. D., Iacono, M. J., & Clough, S. A. (1997). Radiative transfer for inhomogeneous atmospheres: RRTM, a validated correlated-k model for the longwave. *Journal of Geophysical Research*, *102*(D14), 16663–16682. https://doi.org/10.1029/97jd00237

Müller, R. D., Seton, M., Zahirovic, S., Williams, S. E., Matthews, K. J., Wright, N. M., et al. (2016). Ocean basin evolution and global-scale plate reorganization events since Pangea breakup. *Annual Review of Earth and Planetary Sciences*, *44*(1), 107–138. https://doi.org/10.1146/annurev-earth-060115-012211

O'Gorman, P., & Muller, C. J. (2010). How closely do changes in surface and column water vapor follow Clausius–Clapeyronscaling in climate change simulations? *Environmental Research Letters*, *5*(2), 025207. https://doi.org/10.1088/1748-9326/5/2/025207

Pietschnig, M., Lambert, F., Saint-Lu, M., & Vallis, G. (2019). The presence of Africa and limited soil moisture contribute to future drying of South America. *Geophysical Research Letters*, *46*(21), 12445–12453. https://doi.org/10.1029/2019gl084441

Pietschnig, M., Swann, A. L., Lambert, F. H., & Vallis, G. K. (2021). Response of tropical rainfall to reduced evapotranspiration depends on continental extent. *Journal of Climate*, *34*(23), 9221–9234. https://doi.org/10.1175/jcli-d-21-0195.1

Pithan, F., & Mauritsen, T. (2014). Arctic amplification dominated by temperature feedbacks in contemporary climate models. *Nature Geoscience*, *7*(3), 181–184. https://doi.org/10.1038/ngeo2071

Po-Chedley, S., Armour, K. C., Bitz, C. M., Zelinka, M. D., Santer, B. D., & Fu, Q. (2018). Sources of intermodel spread in the lapse rate and water vapor feedbacks. *Journal of Climate*, *31*(8), 3187–3206. https://doi.org/10.1175/jcli-d-17-0674.1

Raper, S. C., Gregory, J. M., & Stouffer, R. J. (2002). The role of climate sensitivity and ocean heat uptake on AOGCM transient temperature response. *Journal of Climate*, *15*(1), 124–130. https://doi.org/10.1175/1520-0442(2002)015<0124:trocsa>2.0.co;2

Scher, H. D., & Martin, E. E. (2006). Timing and climatic consequences of the opening of Drake Passage. *Science*, *312*(5772), 428–430. https://doi.org/10.1126/science.1120044

Schneider, S. H., & Thompson, S. L. (1981). Atmospheric CO2 and climate: Importance of the transient response. *Journal of Geophysical Research*, *86*(C4), 3135–3147. https://doi.org/10.1029/jc086ic04p03135

Scotese, C. R., Gahagan, L. M., & Larson, R. L. (1988). Plate tectonic reconstructions of the Cretaceous and Cenozoic ocean basins. *Tectonophysics*, *155*(1–4), 27–48. https://doi.org/10.1016/0040-1951(88)90259-4

Sejas, S. A., Albert, O. S., Cai, M., & Deng, Y. (2014). Feedback attribution of the land-sea warming contrast in a global warming simulation of the NCAR CCSM4. *Environmental Research Letters*, *9*(12), 124005. https://doi.org/10.1088/1748-9326/9/12/124005

Seton, M., Müller, R. D., Zahirovic, S., Gaina, C., Torsvik, T., Shephard, G., et al. (2012). Global continental and ocean basin reconstructions since 200 Ma. *Earth-Science Reviews*, *113*(3–4), 212–270. https://doi.org/10.1016/j.earscirev.2012.03.002

Shell, K. M., Kiehl, J. T., & Shields, C. A. (2008). Using the radiative kernel technique to calculate climate feedbacks in NCAR's Community Atmospheric Model. *Journal of Climate*, *21*(10), 2269–2282. https://doi.org/10.1175/2007jcli2044.1

Sijp, W. P., & England, M. H. (2004). Effect of the Drake Passage throughflow on global climate. *Journal of Physical Oceanography*, *34*(5), 1254–1266. https://doi.org/10.1175/1520-0485(2004)034<1254:eotdpt>2.0.co;2

Siler, N., Bonan, D. B., & Donohoe, A. (2023). Diagnosing mechanisms of hydrologic change under global warming in the CESM1 large ensemble. *Journal of Climate*, *36*(23), 8243–8257. https://doi.org/10.1175/jcli-d-23-0086.1

Siler, N., Roe, G. H., & Armour, K. C. (2018). Insights into the zonal-mean response of the hydrologic cycle to global warming from a diffusive energy balance model. *Journal of Climate*, *31*(18), 7481–7493. https://doi.org/10.1175/jcli-d-18-0081.1

Soden, B. J., Held, I. M., Colman, R., Shell, K. M., Kiehl, J. T., & Shields, C. A. (2008). Quantifying climate feedbacks using radiative kernels. *Journal of Climate*, *21*(14), 3504–3520. https://doi.org/10.1175/2007jcli2110.1

Stouffer, R. J., & Manabe, S. (1999). Response of a coupled ocean–atmosphere model to increasing atmospheric carbon dioxide: Sensitivity to the rate of increase. *Journal of Climate*, *12*(8), 2224–2237. https://doi.org/10.1175/1520-0442(1999)012<2224:roacoa>2.0.co;2

Stouffer, R. J., Manabe, S., & Bryan, K. (1989). Interhemispheric asymmetry in climate response to a gradual increase of atmospheric CO2. *Nature*, *342*(6250), 660–662. https://doi.org/10.1038/342660a0

Straume, E. O., Gaina, C., Medvedev, S., & Nisancioglu, K. H. (2020). Global Cenozoic paleobathymetry with a focus on the Northern Hemisphere oceanic gateways. *Gondwana Research*, *86*, 126–143. https://doi.org/10.1016/j.gr.2020.05.011

Toggweiler, J., & Samuels, B. (1995). Effect of Drake Passage on the global thermohaline circulation. *Deep Sea Research Part I: Oceanographic Research Papers*, *42*(4), 477–500. https://doi.org/10.1016/0967-0637(95)00012-u

Vallis, G. K., Colyer, G., Geen, R., Gerber, E., Jucker, M., Maher, P., et al. (2018). ISCA, V1. 0: A framework for the global modelling of the atmospheres of Earth and other planets at varying levels of complexity. *Geoscientific Model Development*, *11*(3), 843–859. https://doi.org/10.5194/gmd-11-843-2018

Vicente-Serrano, S. M., Nieto, R., Gimeno, L., Azorin-Molina, C., Drumond, A., El Kenawy, A., et al. (2018). Recent changes of relative humidity: Regional connections with land and ocean processes. *Earth System Dynamics*, *9*(2), 915–937. https://doi.org/10.5194/esd-9-915-2018

Youngs, M. K., Ferrari, R., & Flierl, G. R. (2020). Basin-width dependence of northern deep convection. *Geophysical Research Letters*, *47*(15), e2020GL089135. https://doi.org/10.1029/2020gl089135

Zelinka, M. D., Randall, D. A., Webb, M. J., & Klein, S. A. (2017). Clearing clouds of uncertainty. *Nature Climate Change*, *7*(10), 674–678. https://doi.org/10.1038/nclimate3402